



An induction-coil magnetometer for mid-plane measurements in spectrometer magnets

Melvin Liebsch^{a,*}, Stephan Russenschuck^a, Jens Kaeske^{a,b}

^a European Organization for Nuclear Research, CERN, Meyrin 1211, Switzerland

^b Karlsruhe Institute of Technology, KIT, Karlsruhe 76131, Germany

ARTICLE INFO

Keywords:

Magnetic measurements
Accelerator magnets
Printed circuit boards
Sensor design

PACS:

0000, 1111
2000 MSC: 0000
1111

ABSTRACT

Induction-coil magnetometers are among the most common devices for measuring both static and transient magnetic fields in accelerator and spectrometer magnets. Recent developments have included an induction-coil array mounted on a sledge, which is translated on the mid-plane of normal-conducting spectrometer magnets. This device, subsequently denoted as the moving fluxmeter, is used to derive the field homogeneity in the magnet center, as well as the gradients in the fringe-field areas. Induction coils capture the magnetic flux through the surface that is traced out by the coil windings. A deconvolution is necessary to recover the flux density from the measured voltage signal. The key idea of this article is to combine the advantages of small and large induction coils to optimize the sensitivity function in the frequency domain. In this way, an information loss due to "blind-eye" frequencies can be avoided and signals can be deconvoluted with ease. While the coil design and metrological characterization is inspired by the theory of the rotating-coil magnetometer, the sensitivity function needs to be expressed in terms of longitudinal spatial instead of angular frequencies. Consequentially we are working with Fourier transforms, instead of Fourier series of periodic signals. The coil sensitivity function, i.e., the convolution kernel, is optimized in the relevant frequency range by the precise layout of the coil-turns on a printed circuit board (PCB). Measurement results are presented that validate the concept and prove its advantages with respect to the classical coil design.

1. Introduction

State-of-the-art sensors for the measurement of static magnetic fields in accelerator magnets make use of induction coils built with printed circuit board (PCB) technology. This stems from the high accuracy in the μm range for the track positioning and the accuracy in the $10\ \mu\text{m}$ range for the layer stacking that can be achieved in PCB manufacturing [1].

The application and optimization of printed circuit boards for magnetic measurements by means of rotating coils is state-of-the-art [2] and [3]. These systems are used to characterize the field in cylindrical domains, such as the vacuum pipes of accelerator magnets.

However, mass spectrometers and fragment separators require field-quality measurements in rectangular regions with high aspect ratios. Because rotating coil measurements are not applicable for such domains, a new measurement system has been developed to determine the magnetic field profiles in dipole magnets, by moving the sensors longitudinally through the magnetic field [4].

Integrating the voltage of any rotating or translating induction coil

yields the incremental magnetic flux through the surface that is traced out by the coil windings. This incremental flux can be considered as the convolution of the magnetic flux density with a coil sensitivity function. A deconvolution is therefore necessary to recover the flux density from the measured voltage signals.

For rotating induction-coil measurements, this deconvolution is performed by applying calibration factors to the coefficients of a Fourier series of the measured flux measurements [5]. The optimization of the track layout of a PCB with respect to these calibration factors is well understood, see for instance [1] and [2]. Configurations to increase or decrease the coil sensitivity for certain Fourier coefficients (angular frequencies) have been developed. These advances have increased the accuracy of rotating coil measurements significantly, as it is possible to minimize the susceptibility towards common mode vibrations and variations in angular velocity [2].

In the same way as the sensitivity of rotating coils can be optimized for certain Fourier coefficients (angular frequencies), we will show that the sensitivity of the moving fluxmeter can be improved for certain

* Corresponding author.

E-mail address: melvin.liebsch@cern.ch (M. Liebsch).

longitudinal frequencies. Moreover, we will present a new design technique that avoids vanishing sensitivity (blind eyes) in the relevant frequency band. This not only mitigates information loss but also yields a robust solution for the deconvolution problem.

This paper is structured as follows: In Section 2 we present the coil sensitivity function for the moving fluxmeter and its implications. This coil shape optimization is then carried out in Section 3 based on a particular dipole magnet. Finally, in Section 4 we present an experimental validation of the proposed coil design.

2. The coil sensitivity function

A picture of the moving fluxmeter is shown in Fig. 1. The main component of this system is a PCB which is hosting an array of induction coils (green). This PCB is mounted on a sled that is pulled by a motor in a way that it can be shifted through the air gap of a dipole magnet. The PCB is located in the xz -plane and it is pulled longitudinally along z . A field variation over the coil surface induces a measurable voltage U_{ind} across the coil's connection terminals when moving it through the static magnetic field. A linear encoder is used to generate trigger pulses with the spatial resolution Δz , and the induced voltage is integrated in time between these pulses. In order to avoid "blind spots", between the integration windows, we make use of a fast digital integrator (FDI) [6] for the temporal integration. This results in M measurement positions at the instances t_m with $z(t_m) = z_m = z_0 + m\Delta z$ for $m = 1, \dots, M$. The measured signal $\Delta\Phi(z_m)$ is the flux linked with the surfaces traced out by the leading and lagging edges for the displacement of the coil from z_m to z_{m+1} ; see Fig. 2 bottom:

$$\Delta\Phi(z_m) = w \int_{z_m}^{z_{m+1}} \left[B_y \left(z + \frac{l}{2} \right) - B_y \left(z - \frac{l}{2} \right) \right] dz. \quad (1)$$

The integral on the right-hand side defines the coil's sensitivity in the spatial domain. The sensor length l leads to an objective conflict: The shorter the coil, the less sensitive it is for slowly-varying fields. The longer the coil, the smaller is the sensitivity for rapidly-varying fields.

2.1. The coil sensitivity function in the frequency domain

The quantity of interest, that is, the field component $B_y(z)$, is now expressed in terms of its Fourier transform:

$$B_y(z) = \int_{f=-\infty}^{\infty} (\mathcal{F}B_y)(f) \exp(j2\pi zf) df. \quad (2)$$

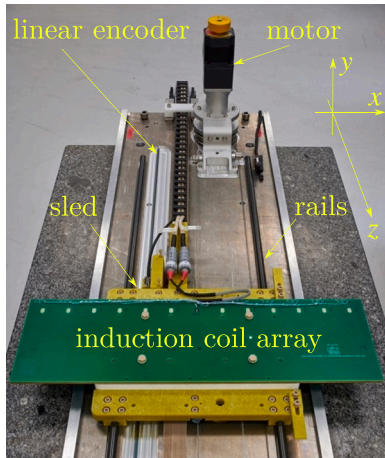


Fig. 1. The moving fluxmeter: an induction-coil array is mounted on a sledge that is guided by rails and pulled by a motor. A linear encoder is used to measure the longitudinal position (z) of the sled.

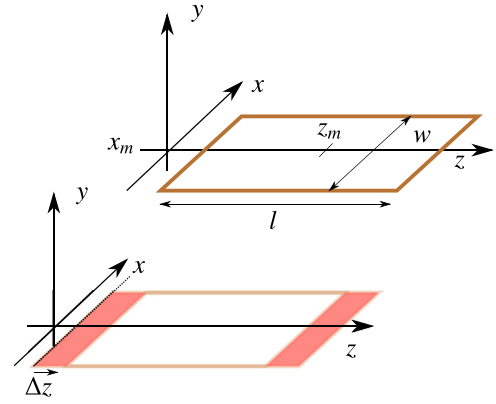


Fig. 2. Top: Rendering of a rectangular coil in the xz -plane. Bottom: The active area of an induction coil moving in the xz -plane.

The flux increment $\Delta\Phi_i$ for a rectangular coil with a single turn of length l_i and width w_i , is expressed in terms of the Fourier transform $\mathcal{F}B_y$, and is given by

$$\Delta\Phi_i(z_m) = w_i \int_{f=-\infty}^{\infty} (\mathcal{F}B_y)(f) s_i(f) df, \quad (3)$$

with the sensitivity function

$$s_i(f) = \frac{\sin(\pi l_i f)}{\pi f} (\exp(j2\pi f \Delta z) - 1) \exp(j2\pi f z_m) \quad (4)$$

see Appendix 6.1.

State-of-the-art induction coils for magnetic measurements are built with printed circuit board (PCB) technology. The coil is wound on several PCB layers by several turns of different lengths and widths w_i , l_i . Denoting by T the number of turns and by N the number of layers,¹ the sensitivity function for the PCB coil follows from eq. (4)

$$s(f) = N \underbrace{\left(\sum_{i=1}^T w_i \frac{\sin(\pi l_i f)}{\pi f} \right)}_{\text{geometric term } s_{\text{geo}}} \underbrace{\exp(j2\pi f \Delta z) - 1}_{\text{integration term } s_{\text{int}}}. \quad (5)$$

This equation serves as the basis for the design of the coil lengths l_i as well as the choice of the optimal trigger distance $\Delta z = z_{m+1} - z_m$. To this end we introduce the geometric term s_{geo} and the integration term s_{int} . In order to obtain non-vanishing flux increments, the following conditions must be obeyed:

$$(1) : l_i \neq \frac{k}{f}, \quad (2) : \Delta z \neq \frac{k}{f}, \quad k \in \mathbb{N}_0. \quad (6)$$

Condition (1) stems from the distance between the leading and lagging edges. Zero values for k/f appear due to spatial frequencies of the field distribution that are multiples of the inverse coil length. The vanishing contribution of such frequencies is also known as the *blind-eye* of the induction-coil magnetometer. The term s_{geo} can be understood as a frequency dependent equivalent coil surface. Indeed, for the limit $f \rightarrow \infty$, the term $\sin(\pi l_i f)/\pi f$ approaches l_i , i.e., s_{geo} corresponds to the total surface spanned by the induction coil for $f \rightarrow 0$.

Condition (2) results from the integration over z between the encoder triggers. Increasing the trigger distance increases the sensitivity for certain frequencies, but care must be taken to avoid additional blind-

¹ The thickness of the device can usually be neglected as modern PCB technology allows for the stacking of several layers within the range of 1 mm. Moreover, the sensor is designed for mid-plane measurements in dipole magnets, where $\partial_y B_y \approx 0$ for symmetry reasons.

eyes for frequencies matching the inverse trigger distance. Notice that this term is zero for $f = 0$, which implies that the induction coil is insensitive to constant fields.

In Figs. 3 and 4 the geometric and integration terms are shown for rectangular induction coils of different parameters. We notice that blind-eyes are shifted to high frequencies for smaller sensors.

However, the sensitivity for $f \rightarrow 0$ decreases. This, however, is the regime where most of the signal power is expected.

Fig. 4 bottom shows that the sensitivity for small frequencies is improved by increasing the trigger distance Δz . However, the spatial resolution is impaired in this case.

2.2. Signal deconvolution

Once the signal $\Delta\Phi(z)$ is measured, the vertical field component $B_y(z)$ can be determined by performing a deconvolution in the frequency domain. Noticing from eq. (2) that the spectrum of the measured signal is $(\mathcal{F}\Delta\Phi)(f) = (\mathcal{F}B_y)(f)s(f)$, the spectrum $(\mathcal{F}B_y)(f)$ can be determined by division in the frequency domain

$$(\mathcal{F}B_y)(f) = \frac{(\mathcal{F}\Delta\Phi)(f)}{s(f)}. \quad (7)$$

The inverse Fourier transformation then yields the signal $B_y(z)$.

Because all induction coils are insensitive to constant fields (see term eq. 2 in eq. (5)), the $(\mathcal{F}B_y)(f=0)$ component needs to be reconstructed using a static magnetic field sensor. To this end, Hall probes and nuclear magnetic resonance sensors may be used, but a good practice is also to determine the constant by setting $B_y = 0$ at $z = 0$ if this position is sufficiently far away from the magnet.

Deconvoluted signals are prone to the amplification of measurement noise in the frequency ranges where the $s(f)$ takes small values. Common solutions to this problem are the filtering of the concerned frequency components or their damping with respect to a known signal to-noise

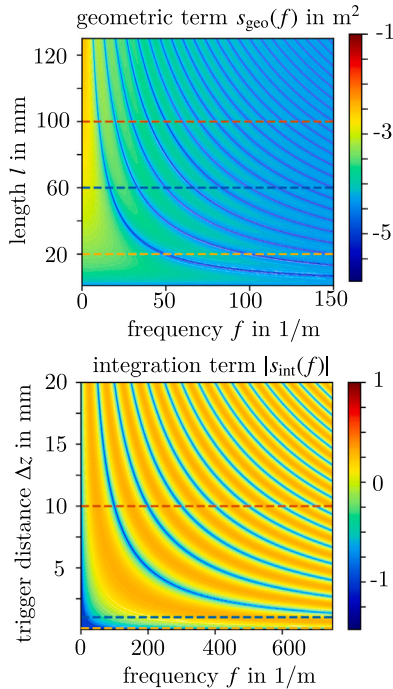


Fig. 3. Geometric and integral terms s_{geo} and s_{int} . Here, a rectangular coil with a single turn of width 30 mm is considered. Top: Absolute value of the geometric term $|s_{\text{geo}}|$ in logarithmic scale over the sensor length and frequency. Bottom: Absolute value of the integral term $|s_{\text{int}}|$ over trigger distance and frequency. In both cases, the colored lines indicate where the curves in Fig. 4 have been evaluated.

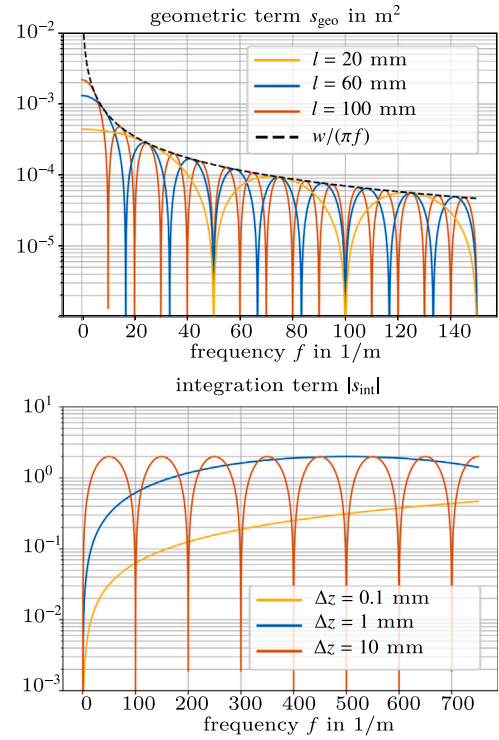


Fig. 4. Top: The geometric term s_{geo} , for a rectangular induction coil with a single turn on a single layer. The width in all cases is 22 mm. The geometric term is shown for different sensor lengths. Bottom: The integration term s_{int} comes from the integration in time between the encoder triggers. The three lines represent $s_{\text{int}}(f)$ for three trigger distances $\Delta z = 0.1, 1$ and 10 mm.

ratio. The latter approach is referred to as Wiener filtering and it has been applied to the deconvolution of rotating coil measurements in [7]. However, all signal filtering or post-processing is either neglecting some frequency components or using prior knowledge for their determination. In the following, we will show that imposing prior knowledge can be avoided by preventing blind-eyes in the sensor design.

3. Coil-shape optimization

3.1. The relevant frequency band

The aim of the coil-shape optimization is to maximize geometric term in the frequency range, required to resolve the field profile. This frequency range must be computed for the magnet to be tested. In the following, a non-saturated dipole magnet is considered and the field profile $B_y(z)$ is taken from a numerical field simulation [8]; see Fig. 5 top. The required frequency range is estimated by truncating the spectrum $(\mathcal{F}B_y)(f)$.

From Parseval's theorem, it is known that the total energy of a signal is equal to the integral over the power spectrum

$$W_{\text{tot}} = \int_{f=-\infty}^{\infty} |\mathcal{F}B_y(f)|^2 df. \quad (8)$$

For the considered signal, nearly all of the signal energy is distributed in a frequency band of $f < 75$ 1/m. This can be seen from the relative energy difference between a truncated signal $W_{\text{trunc}}(f_c)$ and W_{tot} ; $\epsilon(f_c) := 1 - W_{\text{trunc}}(f_c)/W_{\text{tot}}$. Truncating at $f_c = 75$ 1/m yields $\epsilon(f_c) = 9 \cdot 10^{-12}$. The power spectrum $|\mathcal{F}\{B_y\}(f)|^2$ is shown in Fig. 5, bottom. The maximum errors in the truncated signal in the spatial domain are at $20\mu\text{T}$ (see Fig. 5, top).

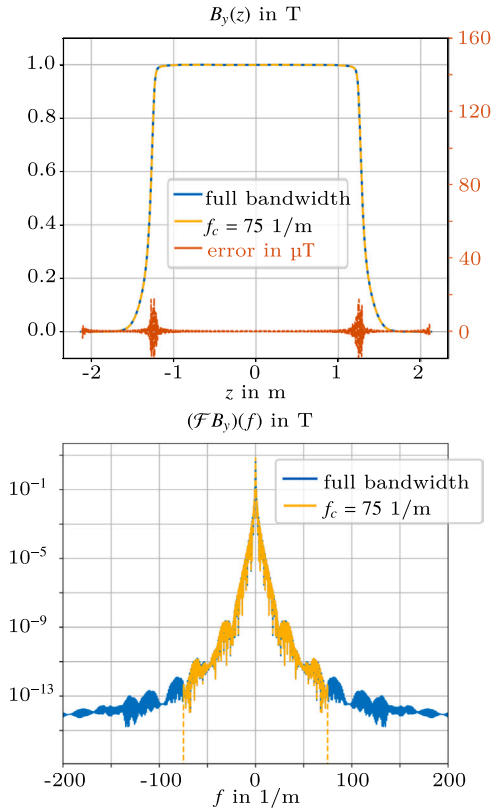


Fig. 5. Profile, power spectrum, as well as the truncated power spectrum of the vertical flux density component B_y in case of a normal-conducting dipole magnet.

3.2. Coil shape optimization

The coil shape is affecting the geometric term s_{geo}

$$s_{\text{geo}}(f) = N \sum_{i=1}^T w_i \frac{\sin(\pi l_i f)}{\pi f}. \quad (9)$$

Having determined the relevant frequency band $f < f_c$, various criteria for optimizing the coil layout are conceivable. One possibility is to specify the function $s_{\text{geo}}(f)$ in the frequency domain and approximate it by superimposing $\sin(\pi l_i f)/\pi f$ pulses. As the coil length appears in the argument of \sin , this yields a nonlinear optimization problem. To simplify the optimization, it makes sense to define design templates, which are parameterized by a small set of design variables. Two design templates are in the center of the following discussion.

Definition 3.1. (The rectangular coil template). Starting from an inner turn of length l_1 and width w_1 , the rectangular coil template uses the scaling laws

$$l_{i+1} = l_1 + i\lambda, \text{ and } w_{i+1} = w_1 + i\lambda. \quad (10)$$

for the length l_i and width w_i of the i -th turn. The parameter $\lambda > 0$ is the PCB track distance.

Definition 3.2. (The graded coil template). Starting from an inner turn of length l_1 and width w_1 , the length of the i -th turn is

$$l_{i+1} = (1 + \nu)l_i = (1 + \nu)^i l_1, \text{ with } 0 < \nu < 1, \quad (11)$$

and the width of the i -th turn is

$$w_{i+1} = w_1 + i\lambda, \lambda > 0, \quad (12)$$

The parameter $\lambda > 0$ is the PCB track distance and the parameter ν is a

recursion parameter.

Remark 1. The graded coil template may be considered as a special case of the more general template with three parameters $(\lambda, \lambda_w, \nu)$, and the scaling laws $l_{i+1} = l_1 + i\lambda + (1 + \nu)^i l_1$, and $w_{i+1} = w_1 + i\lambda_w$. Definition 3.2 follows for $\lambda = 0$. The coil shape optimization based on the three parameter template is reserved for future investigations.

In Fig. 6 we show the layouts of two induction coils, which have been designed by following the two design templates. The coil colored in red is the result of the coil shape optimization and it will be denoted as the graded coil. The blue one is a rectangular induction coil, which was produced for the first generation of the moving fluxmeter. It will be denoted as the rectangular coil.

The benefit of the graded coil template is that it allows us to combine the advantages of small and large induction coils, by tuning a single recursion parameter ν . Moreover, as we will see in the following, it yields a more robust design with respect to track positioning errors in the PCB manufacturing process.

For the inner winding length l_1 one may select the minimum possible coil length, which is typically given due to manufacturing constraints. For instance, the layers on the printed circuit board have to be connected by vias. These vias are usually placed in the middle of the coil and require space.

In Fig. 7 we show the geometric term $s_{\text{geo}}(f)$ for the graded coil template as a function of different recursion parameters ν . In this case the inner winding length l_1 is given by the space required for the vias in the PCB center and is 6.13 mm. The total coil length is $(1 + \nu)^{T-1} l_1$ and it depends on the recursion parameter ν as well as the number of turns T . For $0.25 < \nu < 0.28$ the coil length is in the range of 75–93 mm, when using $T = 12$ turns. Increasing ν increases the coil length and therefore shifts the first blind-eye towards small frequencies. For $\nu = 0.275$, the first blind eye is at $f = 80$ 1/m. This yields a safety margin to the cut-off frequency $f_c = 75$ 1/m.

With a solution of the recursive parameter ν at hand, the question arises how manufacturing errors and tolerances influence the design. To answer this question we study the effect of a small perturbation δl_i on the i -th turn of the induction coil. A first-order Taylor expansion of (17) yields

$$\begin{aligned} & s_{\text{geo}}(f)|_{\delta l_i=0} + \left(\frac{d}{d l_i} s_{\text{geo}}(f) \right)_{\delta l_i=0} \\ &= N \sum_{i=1}^T w_i \frac{\sin(\pi l_i f)}{\pi f} + w_i N \cos(\pi l_i f) \delta l_i. \end{aligned} \quad (13)$$

For the uncertainty quantification we define the zero mean, Gaussian distributed perturbations $\delta l_i \sim \mathcal{N}(0, \sigma_l^2)$ for $i = 1, \dots, T$, which are uncorrelated, i.e. $\mathbb{E}[\delta l_i \delta l_j] = 0$ for i, j . The variance is denoted by σ_l^2 and it is equal for all turns.

With the linearization according to eq. (13) and the linearity of the expected value function $\mathbb{E}[\cdot]$ we find analytical expressions for the mean value

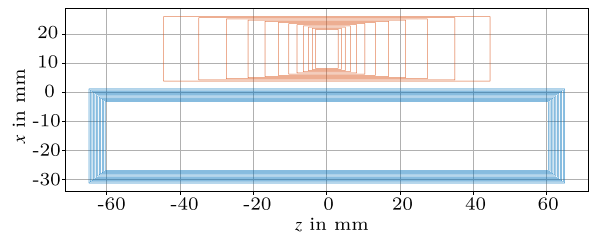


Fig. 6. The layout of the optimal sensor (red) compared to a conventional induction coil (blue). The red coil will be denoted as *graded coil*, whereas the blue coil will be denoted as *rectangular coil*. The geometric parameters of the two coils are summarized in Table 3.

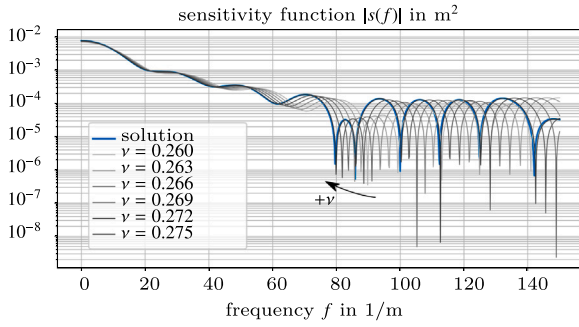


Fig. 7. Optimization of the recursion parameter ν .

$$\mathbb{E}[s_{\text{geo}}(f)] = N \sum_{i=1}^I w_i \frac{\sin(\pi l_i f)}{\pi f} \quad (14)$$

and the variance

$$\text{var}[s_{\text{geo}}(f)] = \sigma_l^2 N^2 \sum_{i=1}^I w_i^2 \cos^2(\pi l_i f), \quad (15)$$

since $\mathbb{E}[\delta l_i \delta l_j] = 0$ for i, j .

The dashed lines in Fig. 8 top illustrate 100 standard deviations $\sigma[s_{\text{geo}}(f)] = \sqrt{\text{var}[s_{\text{geo}}(f)]}$, calculated from on $3\sigma_l = 50 \mu\text{m}$. This means that 99.73 % of all deviations are below $50 \mu\text{m}$, which is a reasonable assumption for modern-day PCB manufacturing.

The logarithmic scale can be misleading in the interpretation of the results. For this reason, we show the relative value $3\sqrt{\text{var}[s_{\text{geo}}]}/s_{\text{geo}}$ in parts per mille in Fig. 8 bottom. Whereas the blue curve (rectangular coil) shows several spikes in the relevant frequency range, no such spikes are appearing for the graded coil (blue). This yields another important advantage of our proposed solution. Avoiding zeros in the sensitivity

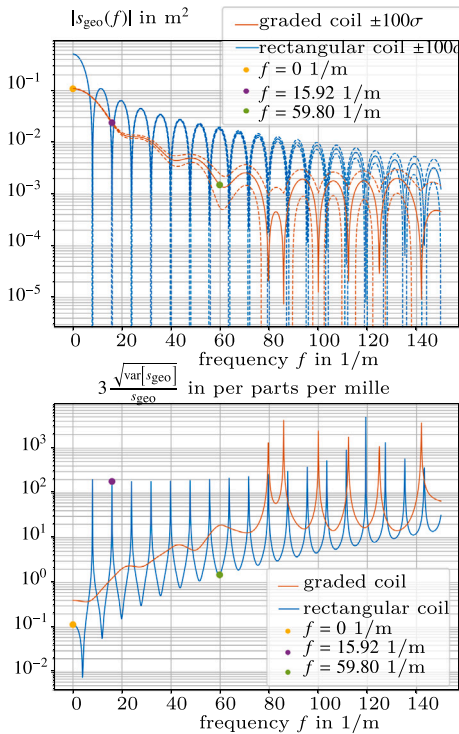


Fig. 8. Top: Sensitivity function $s_{\text{geo}}(f)$ for the graded and rectangular coils. Bottom: s_{geo} Sum over the absolute values of all relative impact functions $\delta_l s_{\text{geo}}(f)$ for all turns $i = 1, \dots, T$.

spectrum results in a more robust design with respect to manufacturing errors.

Remark 2. Deconvolution filters, such as the Wiener filter, are based on the knowledge of the convolution kernel, which is in this case equal to the sensitivity function. As it is seen in Fig. 8, track positioning errors may lead to large differences between the real and the designed sensitivity function. The robustness of the coil design is therefore critical also if more elaborate deconvolution filters are applied.

In Table 1 we give the numerical values for $3\sqrt{\text{var}[s_{\text{geo}}]}/s_{\text{geo}}$ at three frequencies, which are illustrated as dots in Fig. 8. The rectangular coil is preferable for constant fields, but shows significant susceptibility for track positioning errors at the blind-eye frequencies. The largest relative variations for the graded coil are approximately one order of magnitude below the maxima obtained for the rectangular coil.

3.3. The PCB manufacturing

In the previous section we found that the coil layout requires a turn positioning accuracy better than 0.1 mm in order to keep the relative error in the coil surface below one per mille (see Table 1). As this requirement exceeds the capabilities of wound coil manufacturing, the coil must be produced using printed circuit board (PCB) technology, reaching a track positioning accuracy in the $10 \mu\text{m}$ range. A disadvantage of PCB technology is the reduced amount of possible turns because of the minimum feature size, both between layers and between tracks.

The translation sledge, linear encoder, and acquisition system of an existing translating-coil magnetometer are used. This results in constraints for the layout of the PCB and the individual coils as the overall dimensions and the positioning of the mounting holes must be kept identical. The central mounting holes, having a diameter of 7 mm , are used to fix the PCB onto the sledge. Additional holes for dowel pins, with a diameter of 4 mm , are needed for alignment reasons.

The optimized design values of the PCB are given in Table 3. The manufacturing constraints for both designs are given in Table 2. A drawing of the coil layout and an image of the manufactured PCB are shown in Fig. 12.

4. Experimental validation

The graded coil is validated with measurement data. To this end, we compare the performances of the two induction coils shown in Fig. 6. The moving fluxmeter is installed in a normal-conducting dipole magnet of 2.5 m in length. Measurements are performed with both, the graded and the rectangular coils. The total length L of the measured field profile including the fringe field region of the magnet is $L = 4.125 \text{ m}$. Fig. 9 shows a picture of the moving fluxmeter installed in front of the dipole magnet.

For both induction coils we operate the moving fluxmeter with a trigger distance of $\Delta z = 160 \mu\text{m}$. The post-processing of the measurement data is straightforward. It is illustrated as a block diagram in Fig. 13.

Notice that all signal processing is implemented in software and is

Table 1

Three standard deviations relative to the geometric factor in parts per mille. We evaluate the variance and sensitivity function at the frequencies indicated in Fig. 8. The length parameters are randomized with the uncorrelated, zero mean Gaussian perturbations δl_i , with variance $3\sigma_l = 50 \mu\text{m}$.

f in 1/m	$3\sqrt{\text{var}[s_{\text{geo}}]}/s_{\text{geo}}$ in parts per mille	
	graded coil	rectangular coil
0	0.40	0.12
15.92	1.25	181.39
59.80	19.01	1.49

Table 2
Geometric boundary conditions of the new graded coil PCB in comparison to the original, rectangular coil.

Unit	PCB manufacturing constraints					
	Mounting hole distance (longitudinal)	Mounting hole distance (transversal)	Mounting hole diameter	Dowel pin hole diameter	Board width	Board length
Rectangular coil	80	38	7	4	500	150
Graded coil	80	19	7	4	500	150

Table 3
Geometric parameters of the new graded coil layout in comparison to the original, rectangular coil design.

Unit	Geometric PCB parameters						
	Number of turns T	Number of layers N	Inner length l_1	Inner width w_1	PCB track distance λ	Recursion parameter ν	Total coil area m^2
Rectangular coil	12	12	120.9	23.6	0.8	n.a.	0.5063
Graded coil	12	14	6.13	13.4	0.8	0.275	0.1085



Fig. 9. Normal conducting dipole magnet and the moving fluxmeter installed for midplane measurements.

applied on the discrete vector of flux increments $(\Delta\Phi(z_1), \dots, \Delta\Phi(z_M))^T$. All Fourier transformations are approximated by their discrete counterparts.

One key ingredient of our post-processing technique is the band-pass filter, which is used to suppress the $f = 0$ component as well as the frequencies $f > f_c$. We then perform the deconvolution simply by division in the Fourier domain. In the last step, an offset correction is necessary, since we have suppressed the $f = 0$ component of the signal. In this case, we set $B_y(z = 0)$ to zero, as the induction coil at this position is sufficiently far away from the magnet.

We emphasize that this post-processing technique does not require a numerical summation of the flux increments, as it is usually performed

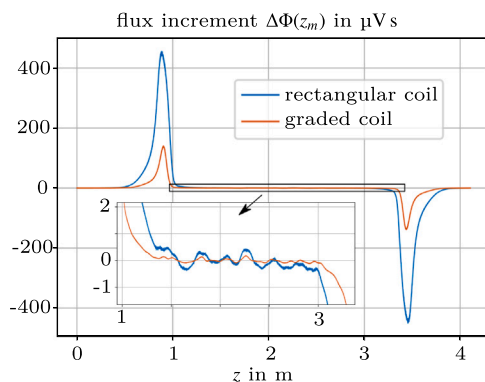


Fig. 10. Measured flux increments for the rectangular and graded coils.

for rotating and translating coil measurements.

In Fig. 10 we show the flux increments measured by the two coils. As the total surface of the rectangular coil is five times larger as the one of the graded coil (see Table 1), also the flux increments are systematically larger by this amount. However, the amplification of sensor noise at the blind eye frequencies of the rectangular coil is clearly visible in the reconstruction of the vertical field component B_y in Fig. 11. This amplification yield spurious oscillations in B_y with amplitudes of ≈ 0.5 mT. The reconstruction based on the graded coil does not show these effects, which validates our design.

It is of course possible to apply more elaborate signal filtering to solve issues related to blind-eye frequencies in the deconvolution. However, with the sensor design presented in this work, this additional post-processing step is not necessary.

5. Conclusion

In this paper we have presented a new induction-coil design for a translating-coil magnetometer for midplane measurements in spectrometer magnets. The sensor is optimized in a way that its sensitivity function gives a flat spectrum in the required spatial frequency range. In this way, information loss due to blind-eye frequencies in the sensor spectrum can be avoided. This improves the robustness for the reconstruction of flux densities with respect to measurement and manufacturing errors and simplifies the deconvolution step in the signal post-processing. The induction-coil magnetometer was optimized with respect to the field distribution of a reference dipole magnet, but the

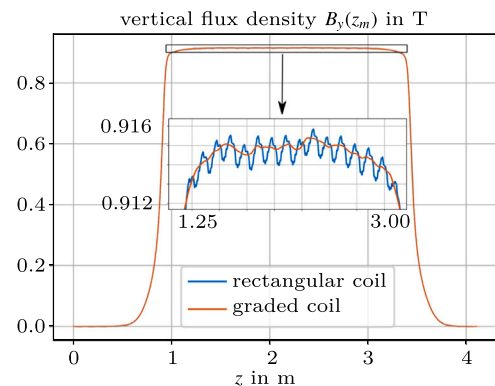


Fig. 11. Vertical field component reconstructed by the postprocessing technique shown in Fig. 13.

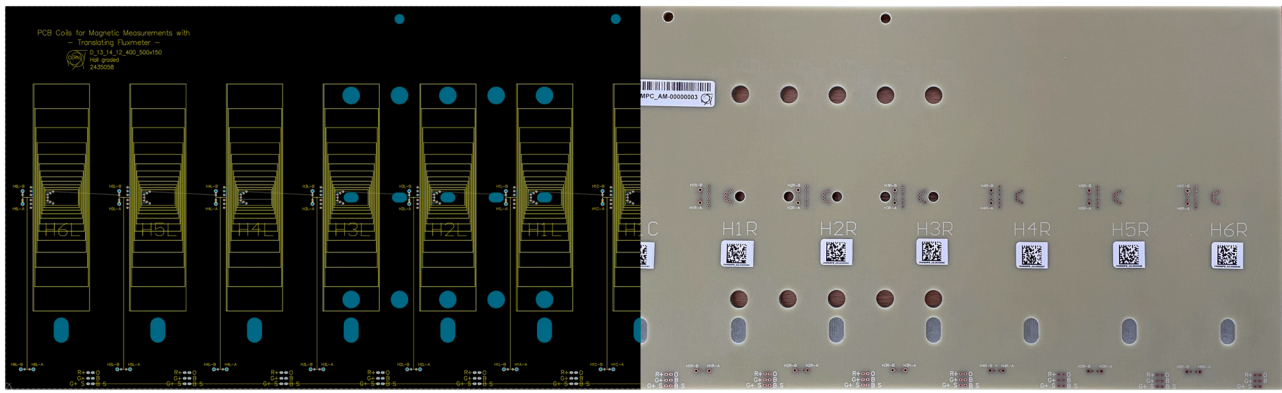


Fig. 12. Optimized PCB layout. CAD rendering (left), manufactured PCB (right). There are 13 coils on the PCB to cover a horizontal extension of 500 mm.

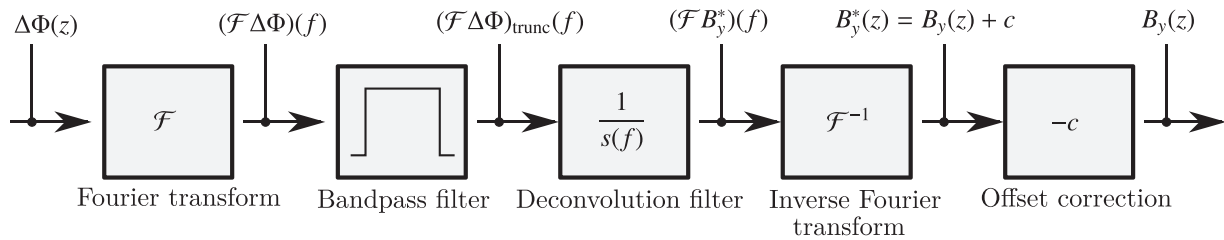


Fig. 13. Measurement data post-processing. Here we illustrate the processing in terms of continuous signals. The real analysis is performed in software, based on the sampled signal $(\Delta\Phi(z_1), \dots, \Delta\Phi(z_M))$. All transformations are applied by means of their discrete counterparts.

principle can be applied easily to other frequency ranges or field distributions.

An interesting application for the proposed coil design would be the field quality measurement in undulator and wiggler magnets. The sensitivity function in the frequency domain could be designed to have vanishing sensitivity for the undulator frequency. This principle is well established for multipole measurements using rotating coils, where it is known as *bucking*.

The moving fluxmeter is currently being used for a measurement campaign. More detailed reproducibility studies are pending.

The measurement data and algorithms used for this publication are accessible in a git-lab repository [9].

Declaration of Competing Interest

The authors declare that they have no known competing financial interests or personal relationships that could have appeared to influence the work reported in this paper.

Data availability

All data and algorithms are available at: <https://gitlab.cern>.

Appendix

Derivation of the coil sensitivity function

Substituting eqs. (10) in (9) yields

[ch/te-msc-mm/inductioncoilmagnetometer](https://gitlab.cern/ch/te-msc-mm/inductioncoilmagnetometer).

Acknowledgments

The work of Melvin Liebsch is supported by the Graduate School CE within the Center for Computational Engineering at Technische Universität Darmstadt. This work has been sponsored by the Wolfgang Gentner Program of the German Federal Ministry of Education and Research (grant no. 13E18CHA).

CRediT authorship contribution statement

Melvin Liebsch: Conceptualization, Data curation, Formal analysis, Investigation, Methodology, Software, Validation, Visualization, Writing - original draft, Writing - review & editing. **Stephan Russenschuck:** Resources, Supervision, Project administration, Funding acquisition, Writing - review & editing. **Jens Kaeske:** Methodology, Validation, Investigation, Data curation, Writing - original draft.

$$\begin{aligned}
\Delta\Phi(z_m) &= \int_{f=-\infty}^{\infty} (\mathcal{F}B_y)(f) \int_{z=z_m}^{z_{m+1}} \exp\left(j2\pi f\left(z + \frac{l}{2}\right)\right) \\
&\quad - \exp\left(j2\pi f\left(z - \frac{l}{2}\right)\right) dz df \\
&= \int_{f=-\infty}^{\infty} (\mathcal{F}B_y)(f) \frac{1}{j2\pi f} \left[\exp\left(j2\pi f\left(z + \frac{l}{2}\right)\right) \right. \\
&\quad \left. - \exp\left(j2\pi f\left(z - \frac{l}{2}\right)\right) \right]_{z_m}^{z_{m+1}} df \\
&= \int_{f=-\infty}^{\infty} (\mathcal{F}B_y)(f) \frac{\sin(\pi lf)}{\pi f} (\exp(j2\pi fz_{m+1}) \\
&\quad - \exp(j2\pi fz_m)) df.
\end{aligned} \tag{24}$$

Where we have used

$$\sin(\pi lf) = \frac{\exp(j\pi lf) - \exp(-j\pi lf)}{2j}. \tag{16}$$

We then substitute $z_{m+1} = z_m + \Delta z$, where Δz is the trigger distance and factor out the expression $\exp(j2\pi fz_m)$ to obtain Eq. (11).

References

- [1] J. DiMarco, G. Severino, P. Arpaia, Calibration technique for rotating PCB coil magnetic field sensors, *Sens. Actuators A: Phys.* 288 (2019) 182–193, <https://doi.org/10.1016/j.sna.2019.02.014> (URL), (<https://www.sciencedirect.com/science/article/pii/S0924424718316054>).
- [2] P. Arpaia, G. Caiafa, S. Russenschuck, A flexible printed-circuit coil for scanning transversal magnetic fields errors in accelerator magnets, *Sens. Actuators A: Phys.* 295 (2019) 193–199, <https://doi.org/10.1016/j.sna.2019.05.038>. URL: (<https://www.sciencedirect.com/science/article/pii/S0924424718320740>).
- [3] P. Rogacki, A contribution to the development and characterization of rotating-coil magnetometers, Dissertation, RWTH Aachen University, Duren, deutsche und englische Zusammenfassung. - Druckausgabe: 2022. - Auch veröffentlicht auf dem Publikationsserver der RWTH Aachen University; Dissertation, RWTH Aachen University, 2021 (2022). doi:10.18154/RWTH-2022-03586. URL (<https://publications.rwth-aachen.de/record/844012>).
- [4] S. Russenschuck, Rotating- and translating-coil magnetometers for extracting pseudo-multipoles in accelerator magnets, *COMPEL* 36 (5) (2017) 1552–1567, <https://doi.org/10.1108/COMPEL-02-2017-0059>.
- [5] S. Russenschuck, *Field Harmonics*, John Wiley & Sons, Ltd, 2010, pp. 237–268.
- [6] P. Arpaia, L. Bottura, P. Cimmino, D. Giloteaux, A. Masi, J.G. Perez, G. Spiezia, L. Walckiers, A fast digital integrator for magnetic field measurements at CERN, In: *Proceedings of the 2006 IEEE Instrumentation and Measurement Technology Conference*, 2006, pp. 67–71. doi:10.1109/IMTC.2006.328175.
- [7] S. Russenschuck, G. Caiafa, L. Fiscarelli, M. Liebsch, C. Petrone, P. Rogacki, Challenges in extracting pseudomultipoles from magnetic measurements, *Int. J. Mod. Phys. A* 34 (36) (2019), 1942022.
- [8] S. Russenschuck, *Field Computation for Accelerator Magnets Analytical and Numerical Methods for Electromagnetic Design and Optimization*, John Wiley & Sons, New York, 2011.
- [9] M. Liebsch, J. Kaeske, TE-MS-C-TM/inductioncoilmagnetometer/gitlab URL: (<https://gitlab.cern.ch/te-msc-mm/inductioncoilmagnetometer>).

Melvin Liebsch received his doctorate in engineering from the Technical University of Darmstadt in 2022. During his Ph.D. period, Melvin Liebsch was working at the Test and Measurement (TM) section within CERN's technology department, where he developed sensor systems and post-processing techniques for magnetic measurements for normal and superconducting accelerator magnets. In his Ph.D. work, Melvin Liebsch used Hybrid Modeling and Bayesian inference techniques to develop a new framework for the post-processing of magnetic measurement data. The data-driven numerical field models obtained in this way, are exploiting the advantages of Boundary Element Methods (BEM) in terms of the smooth reconstruction of the magnetic field.

Stephan Russenschuck received his doctorate in electrical engineering from the Technical University of Darmstadt, specializing in optimization of electrical machines. He joined the European Organization for Nuclear Research (CERN) in 1991 to work on the electromagnetic design of superconducting magnets for the LHC. During the years of LHC development and construction he was responsible for the construction of a model magnet, electrical quality assurance during hardware installation, and the polarities of the nearly 11 000 magnet elements. He is the author of the ROXIE program package and a leading authority on mathematical optimization, electromagnetic design and engineering of accelerator magnets.

Jens Kaeske obtained his master's degree in the field of mechanical engineering from the Karlsruhe University of Technology in 2021. He specialized in the field of mechatronics and microsystem technologies during his studies. Currently, he is pursuing his doctorate at the IPEK institute at KIT in cooperation with the European Organization for Nuclear Research (CERN) in Geneva. During his PhD project he is analyzing and optimizing the development process of superconducting magnets and magnetic transducer.